CANADIAN JOURNAL OF EXPLORATION GEOPHYSICS
VOL. 27, NO 1 (DECEMBER 1991), P. 34-42

A MODEL STUDY OF MULTICHANNEL REFLECTION SEISMIC IMAGING OVER SHALLOW PERMAFROST IN THE BEAUFORT SEA CONTINENTAL SHELF[1]

D.F. POLEY[2] AND D.C. LAWTON[3]

ABSTRACT

Numerical models, developed from permafrost-affected areas of the Beaufort Sea continental shelf, demonstrate that the shallowest high-velocity layer has a profound effect on traveltimes and incidence angles of raypaths for deeper interfaces. Results indicate several factors that make imaging difficult in this type of environment. Firstly, the moveout of reflections is incorrectly modelled by the approximations used in most velocity analyses and moveout correction algorithms to a considerable depth below the high-velocity contrasts. Secondly, tuning of reflections makes separation of events during NMO correction and velocity analysis difficult or impossible. Finally, basal reflections from high-velocity layers can actually cross and arrive before the direct wave, exhibiting both the linear appearance and the apparent velocities appropriate to refractions from the top of the layer. The imaging problem is further complicated if the shallowest high-velocity layer is laterally discontinuous. An understanding of these factors can aid in recording geometry design, processing and interpretation of data recorded in similar environments. High multiplicity at near offsets and severe muting of far-offset data is necessary for imaging of shallow velocity contrasts.

INTRODUCTION

In many areas of the world the quality of both high-resolution and conventional reflection seismic data is detrimentally affected by the presence of shallow large velocity heterogeneities. An entire workshop at the Canadian Society of Exploration Geophysicists 1989 Annual Meeting was dedicated to "Data Acquisition in Problem Areas". Examples of geologies discussed included volcanic rock layers, karst topography, permafrost layers and hard water bottoms, all of which involve large velocity contrasts in the near surface.

In an earlier paper, Poley et al. (1989) used elastic modelling and a real data example from the Beaufort Sea continental shelf to explain poor coherence on reflections from the top and bottom of a single high-velocity frozen layer below the sea bed. In that paper it was demonstrated that amplitude and phase variations on these events in the shot and common midpoint domains can cause standard velocity analyses and stacking techniques to produce erroneous results when applied to these data.

In this paper we use numerical modelling of multichannel seismic reflection data to consider the case of two high-velocity layers and to demonstrate the effect of the shallowest layer on the reflection attributes of deeper interfaces. These results are compared to the case of a single high-velocity layer discussed by Poley et al. (1989). Some of the problems that inhibit imaging within and below high-velocity layers are demonstrated.

Previous work

The presence of several hundred metres of permafrost under most of the Beaufort Sea continental shelf was first predicted by MacKay (1972). An understanding of the distribution and nature of the frozen sediments on the shelf is important both because of geotechnical engineering reasons related to hydrocarbon development and because multichannel seismic data quality is severely affected by its presence.

Initial work concentrated on mapping the areal distribution of ice-bearing sediments on the shelf using refraction seismic surveys (Hunter et al., 1974; Neave et al., 1978; Morak et al., 1983) and high-resolution single-channel reflection seismic profiling (Blasco and O'Connor, 1981; O'Connor and Associates, 1984).

Methods such as multichannel seismic velocity analysis (Hatlelid and MacDonald, 1982), conventional wireline logging in exploration wells (Hnatnik and Randall, 1977; Osterkamp and Payne, 1981), and crystal cable surveys (Walker and Stuart, 1976) have been used to map the total thickness of

[1]Presented at the C.S.E.G./C.S.P.G. National Convention, Calgary, Alberta, June 13, 1989. Manuscript received by the Editor September 10, 1990; revised manuscript received June 1, 1991.

[2]Formerly, Department of Geology and Geophysics, The University of Calgary, Calgary, Alberta, T2N 1N4; presently, Shell Canada Ltd., P.O. Box 100, Stn. M, Calgary, Alberta T2P 2H5

[3]Department of Geology and Geophysics, The University of Calgary, Calgary, Alberta T2N 1N4

The authors thank the Panel on Energy Research and Development, Task 6: Conventional Energy Systems, for funding these studies, as well as Mr. Steve Blasco for administering the project and providing valuable assistance throughout.

ice-bearing permafrost on land-based sites of the Tuktoyaktuk Peninsula.

The Earth Physics Branch of the Department of Energy, Mines and Resources (1983) used available downhole logs from 161 wells to outline permafrost thickness and/or gas hydrate occurrences offshore on the continental shelf. Though this study gave some indication of the overall thickness of permafrost-affected sediments, no attempt was made to discern the internal structure of the permafrost body. Knowledge of overall thickness is not sufficient to provide for reasonable reflection seismic data quality, and further understanding of the spatial relationships between frozen and unfrozen sediments and their effect on multichannel data is required (Poley, 1987).

Fortin (1991) completed a review of published works, reports of several proprietary well site surveys, and permafrost studies in order to map the depth distribution and occurrence, as well as the structure, of frozen sediments. Ice-Bearing-Permafrost (IBPF) is defined as ground that is frozen and has sufficient ice content to result in a measurable change in physical properties, particularly electrical resistivity and acoustic velocity. Results of these studies indicate that on a scale of the entire Beaufort Sea continental shelf, the IBPF body is elongate in a southwest-northeast orientation and is largely controlled by the distribution of deltaic sands. A representative part of one of their cross-sections is shown in Figure 1. The section depicts six main IBPF layers of variable lateral and vertical extent. Of particular interest to this study are what Fortin (1991) defines as the D6 and D5 layers. Unfrozen zones, called taliks, in the top of permafrost on the Mackenzie Delta are formed where lakes and rivers insulate the underlying soils (Smith, 1976). Most of the IBPF sediments offshore are believed to be relic land-based permafrost which formed during long periods of subaerial exposure to low arctic temperatures. Unfrozen areas between adjacent patches of the shallow hummocky layer (D6) have often been recognized as being coincident with shallower

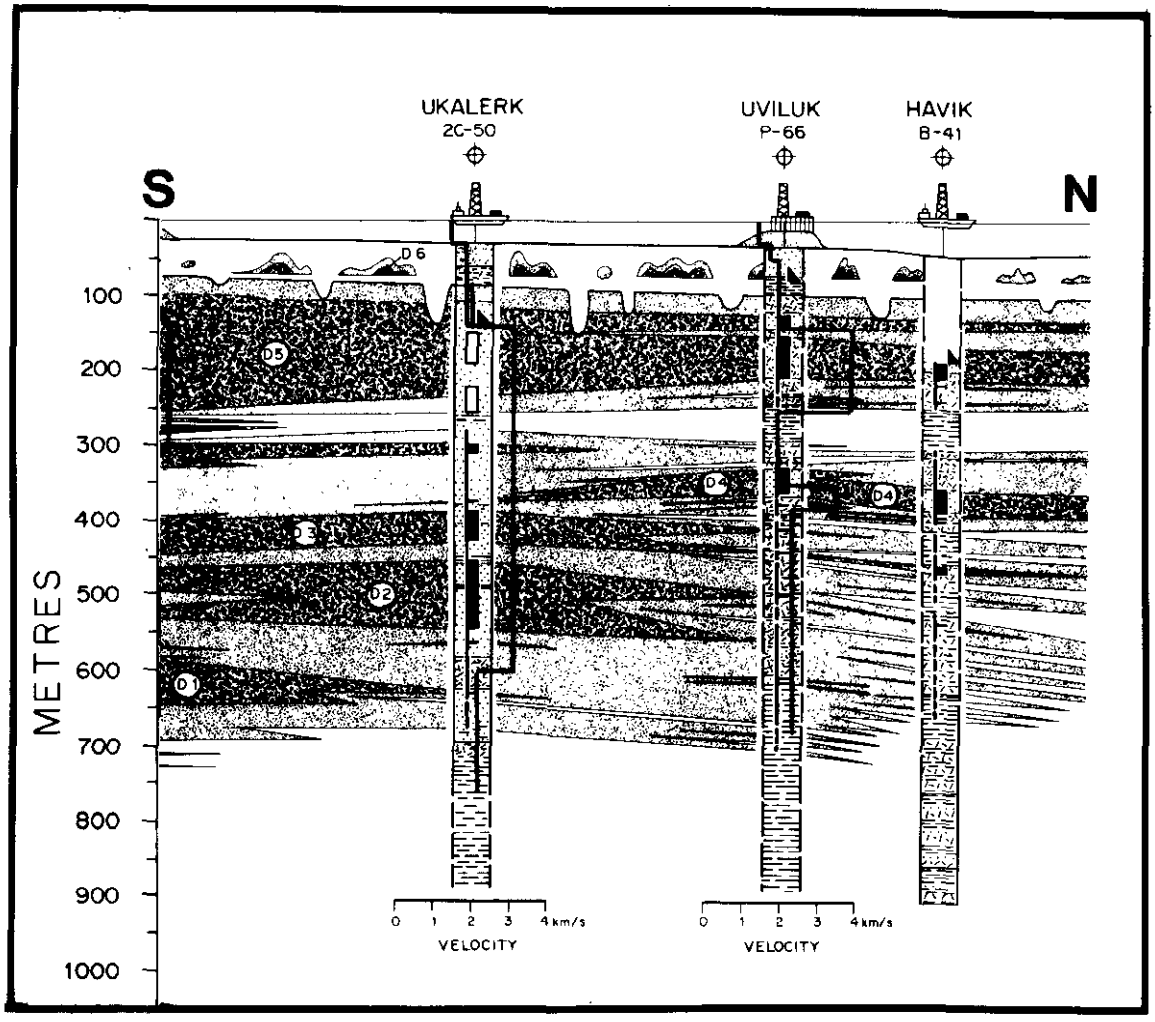

Fig. 1. S-N cross-section of the structure of the IBPF body in the Beaufort Sea continental shelf interpreted from the electrical and sonic logs of the wells shown (after Fortin, 1991). Six main bodies of IBPF have been recognized and are numbered D1 through D6 from depth to surface.

channel or lake deposits. Fortin (1991) indicates that these taliks often extend down into the top of the D5 layer (Figure 1). He also indicates that the bases of both the D6 and D5 layers often coincide with major lithologic changes from coarse-grained to fine-grained sediments and can therefore be abrupt. They note a direct correlation between areas of poor reflection seismic data and thick sequences of IBPF.

The common-midpoint (CMP) technique for the acquisition of reflection seismic data is unsuited to IBPF areas because the method relies on a geometry which provides a small range of incidence angles on reflecting horizons (i.e., small receiver aperture relative to the depths of interest) and small differences in velocity across boundaries. These assumptions often do not apply in the Beaufort Sea where typical streamer lengths for high-resolution multichannel data (600 m) are often longer than depths of interest and where large vertical and lateral contrasts in velocity occur (Poley et al., 1989). This paper focuses on gaining an understanding of some of the specific reasons why reflection seismic data in these areas are poor and how they could be improved. Results from two models will be compared in order to determine the effects of the laterally discontinuous D6 layer on imaging deeper interfaces. This applies to most of the eastern continental shelf according to Fortin (1991) and O'Connor and Associates (1984).

Modelling

Two depth models, depicted in Figure 2, were developed for this study. Model 1 represents a single-IBPF-layer case and is shown on the left side of Figure 2; model 2 represents the 2-IBPF-layer case and is shown on the right side of Figure 2. Details of the two models are presented in Tables 1 and 2.

Model 1 was developed by Poley et al. (1989) and corresponds to an area where a talik has thawed through D6 into the top of D5. Hence, the shallowest IBPF layer is D5 (Figures 1 and 2). Model 2 corresponds to an area where D6 and D5 are both present. The layers encompassing D6 and D5 in Figure 2 represent nonice-bearing sediments. Poisson's ratios for the nonice-bearing layers were estimated from Hamilton (1976) and, for the ice-bearing layers, from both modelling real data (Poley et al., 1989) and results of laboratory tests (Timur, 1968; King et al., 1982).

The recording geometry used in the modelling was a 48-trace record with a group interval of 12.5 m and a near offset of 75 m. These parameters are typical of high-resolution Beaufort Sea programs (Poley, 1987).

Effect of D6 on D5 reflection amplitude and phase

We first consider the effect of the presence of the shallowest IBPF layer (D6) on the amplitude and phase variations of the *P*-wave reflection from the top and bottom of the deeper IBPF layer (D5). Raypaths for the nearest (75 m) and farthest (662.5 m) traces are plotted in Figure 3a for the *P*-wave reflection from all interfaces in model 1. For comparison, the corresponding raypaths for model 2 are shown in Figure 3b. These raypaths show the limits of angles and apertures for the recording geometry used in these models. For the far-trace reflection from

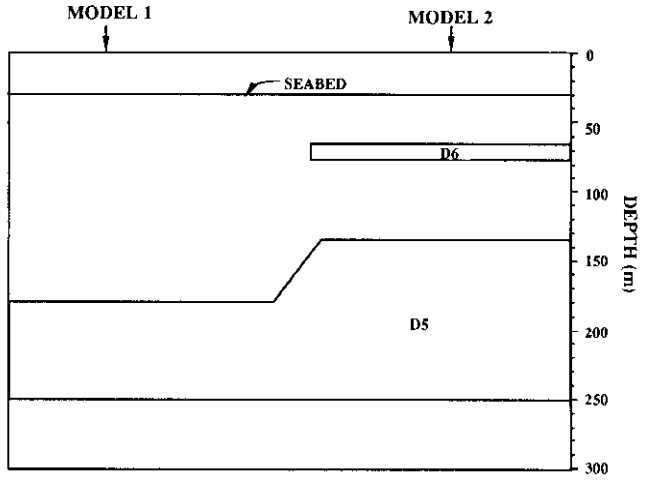

Fig. 2. Schematic diagram of the shallow permafrost distribution showing the thaw talik through D6 into the top of D5. Model 1 and model 2 (Tables 1 and 2) represent the two vertical IBPF distributions of this study.

Table 1. Model 1; single-IBPF layer.

Layer no.	*P* velocity (m/s)	*S* velocity (m/s)	Poisson's ratio	Density (g/cm^3)	Thickness (m)
1	1480	0	0.50	1.0	30
2	1670	681	0.40	2.3	150
3	3500	2020	0.25	2.0	70
4	2000	961	0.35	2.5	halfspace

Table 2. Model 2; two-IBPF layers.

Layer no.	*P* velocity (m/s)	*S* velocity (m/s)	Poisson's ratio	Density (g/cm^3)	Thickness (m)
1	1480	0	0.50	1.0	30
2	1670	681	0.40	2.3	35
3	3500	2020	0.25	2.0	10
4	1670	681	0.40	2.3	60
5	3500	2020	0.25	2.0	115
6	2000	961	0.35	2.5	halfspace

the top of D5, the angle of incidence is much smaller in Figure 3b than in Figure 3a. This is due to the refraction of the ray in the shallower IBPF layer (D6).

Figures 4a and 4b are graphs of *P*-wave reflection incidence angle versus source-receiver offset for the interfaces in models 1 and 2, respectively. For the latter case, the highest incidence angles occur for reflections from the base of the D6 layer and reach values of almost 90 degrees. Another significant aspect of these graphs are the curves for the top of D5 (open squares on both graphs). When D6 is absent, incidence angles range well past the critical angle (28 degrees), so that amplitude and phase variations for the reflection from this layer are

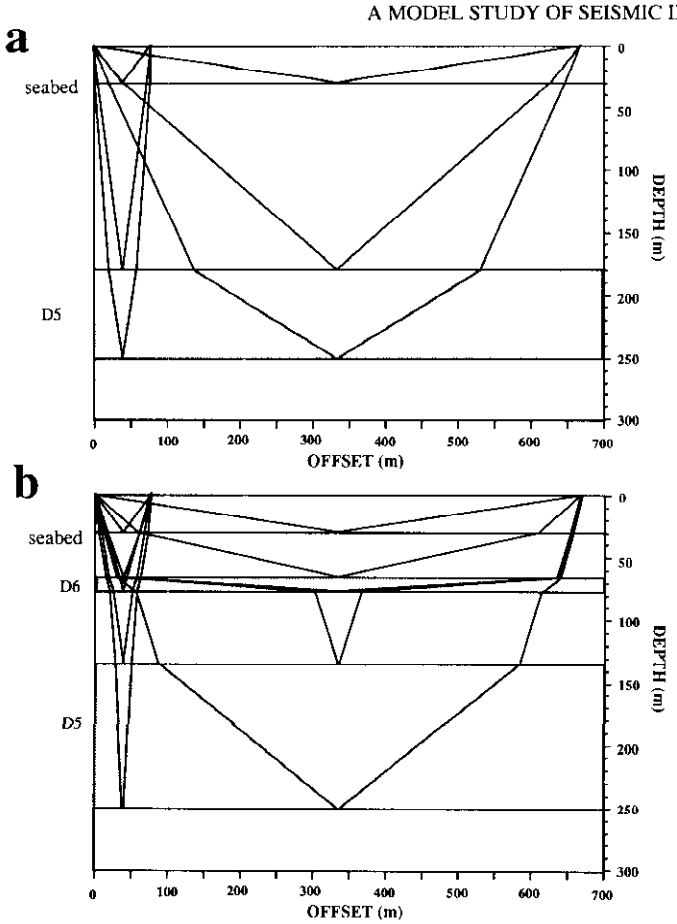

Fig. 3. Select raypaths for the nearest (75 m) and farthest (662.5 m) traces for model 1 **(a)** and model 2 **(b)** and the recording geometry used for the synthetic seismograms in this paper.

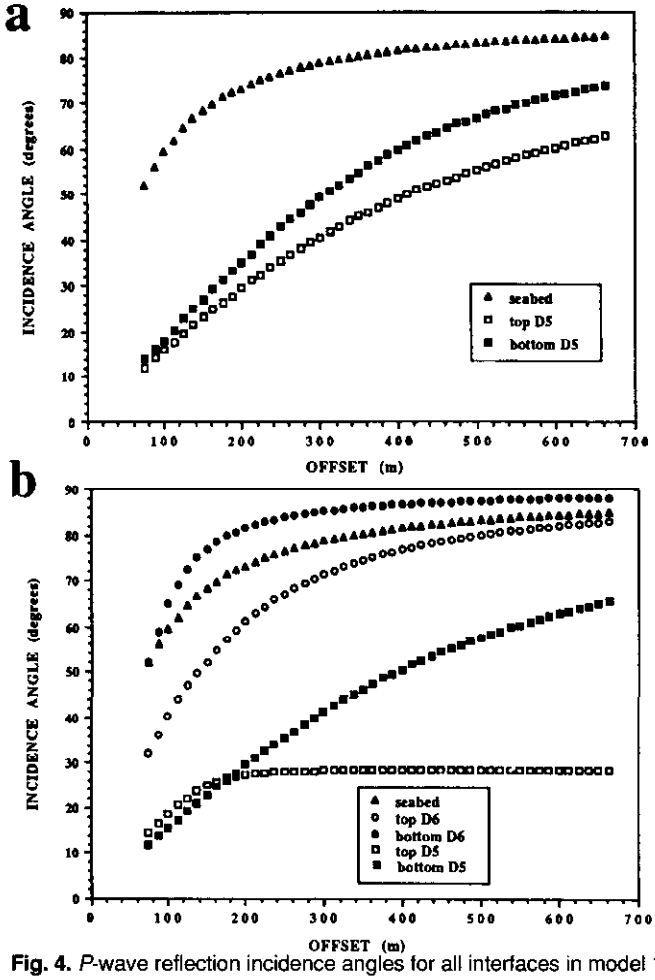

Fig. 4. *P*-wave reflection incidence angles for all interfaces in model 1 **(a)** and model 2 **(b)** and the recording geometry used in synthetic seismograms in this paper.

considerable (Poley et al., 1989). In contrast, where D6 is present, the incidence angles cover a much smaller range and tend to a constant value (near the critical angle) beyond offsets of 200 m.

Synthetic seismograms were generated for models 1 and 2 using a convolutional model and ray tracing to obtain traveltimes. Reflection amplitude and phase were computed using plane wave solutions to the Zoeppritz equations provided by Aki and Richards (1980). To match typical field data, a 70-Hz wavelet was used in the model. The synthetic seismogram for model 1 is shown in Figure 5a and that for model 2 is shown in Figure 5b. It is difficult to differentiate individual reflections in the seismograms due to the interference of various events with the direct arrival. Similar effects are seen in field records (Poley, 1987).

The synthetic seismogram in Figure 6 was calculated by ray tracing model 2 but shows only the reflection from the top of D5 and its corresponding amplitude-versus-offset curve. It is apparent that the amplitude variations with offset for the reflection from the top of D5 are masked when D6 is present. Though incidence angles are mostly constant and near the critical angle (Figure 4b), the amplitude of the reflection decreases with offset and there is no visible phase change. This reflection does not exhibit the large range of amplitude and phase variations observed when D6 is not present (Figure 5a). Gassaway (1984) suggests that amplitude variations with angle of incidence can be masked for a given interface because shallower interfaces remove an increasing fraction of energy as their reflectivity and transmissivity changes with source-receiver offset. Another significant factor has been demonstrated here. When a shallow high-velocity layer overlies layers of lower velocity, the range in angles of incidence on deeper interfaces will be greatly reduced in comparison to when the high-velocity layer is absent. In model 2, reflections from the deeper layer are restricted to sub- or near-critical incidence and do not include the larger amplitude variations associated with either critical angle when a shallower high-velocity layer is not present. The overall magnitude of the reflection from the top of D5 is also smaller when D6 is present, than when it is not, due to the transmission losses caused by D6 above.

The second phase of the modelling was to determine how the depth and thickness of D6 affect the incidence angle, and therefore the amplitude and phase variations, on reflections from the top and bottom of D5. Figures 7 and 8 demonstrate the effect of varying the depth and thickness of a layer of shallow IBPF on the amplitude and incidence angle variations with source-receiver offset. Surprisingly, varying the depth of a 10-m thick D6 layer from 35 to 70 m makes virtually no difference to the amplitude and incidence angle-versus-offset curves for the reflection from the top of D5 (Figure 7). These

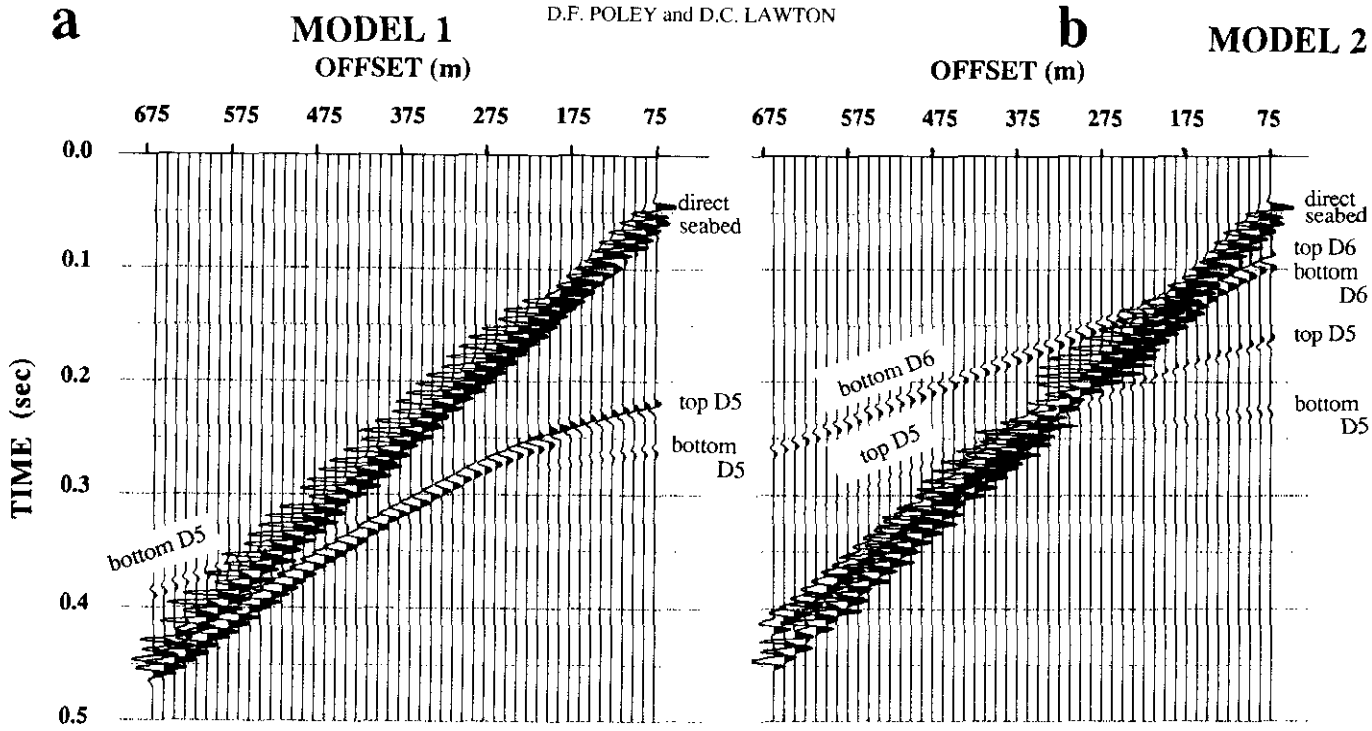

Fig. 5. Synthetic seismograms for *P*-wave reflections from all interfaces in model 1 **(a)** and model 2 **(b)** as well as the direct arrival. Recording geometry is the same as that used in Figures 3 and 4.

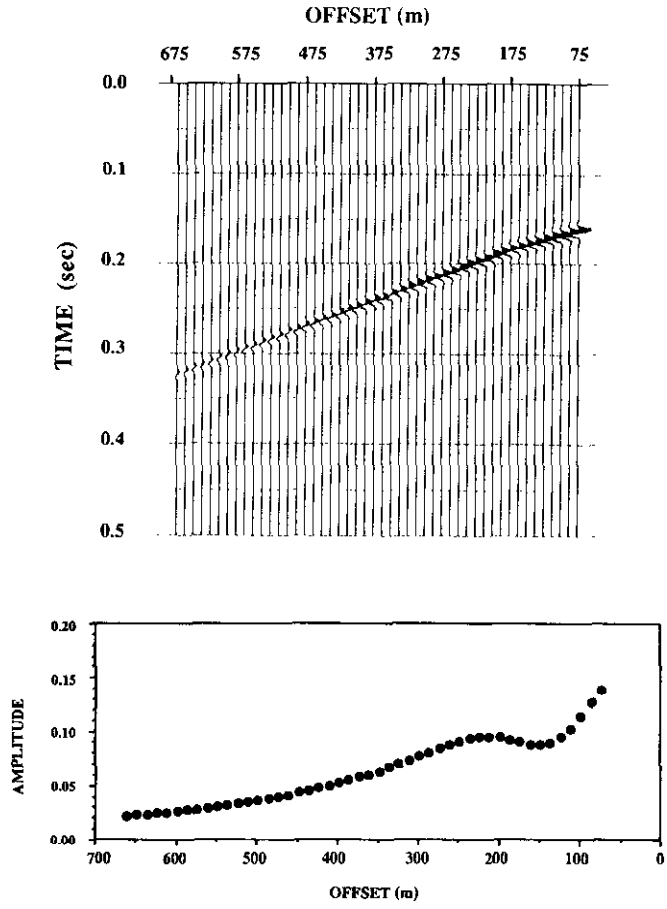

Fig. 6. Synthetic seismogram and corresponding amplitude versus source-receiver offset curve for the *P*-wave reflection from the top of D5 in model 2.

depth ranges are small relative to streamer lengths. Some variation is evident in the amplitude-versus-offset curves when the thickness of the D6 layer is varied (Figure 8), but it is very small (0.08) relative to the amplitude variation on the reflection from D5 when D6 is not present (0.6 in Poley et al., 1989). The maximum incidence angle difference is only 6 degrees. The differences in amplitude on stacked data due to changes in the thickness of D6 may be subtle. Hence, the primary factor controlling amplitude-offset effects and ranges of incidence angles for deeper reflectors is the presence of the shallow layer of permafrost, and much less so its thickness or depth.

Timing of events

The synthetic seismogram for model 2 (Figure 5b) also reveals two additional observations. Firstly, the arrival time of the near-trace reflection from the top of D5 is 70 ms earlier than that for D5 when D6 is not present (Figure 5a). This is partly because the talik has melted the top of D5 (Figure 2). It is also partly due to the static shift (pull-up) of this event caused by the high-velocity D6 layer above. Secondly, there are two arrivals which come in earlier than the direct arrival over a large part of the record.

The reflections from the top and bottom of D6 and D5 in model 2 are shown in Figure 9. At the far-offset trace, the reflection from the base of D6 arrives 150 ms earlier than that from the top, and well before the direct arrival (Figure 9a). At near traces, this reflection is not distinguishable from the reflection from the top of D6 due to interference between the events. Common processing practice is to zero (mute) the traces from zero time to just past the direct arrival. For these data only the four nearest traces would retain the reflection from the top and bottom of D6 and tuning of the two reflections makes them indistinguishable from each other. Conventional normal-

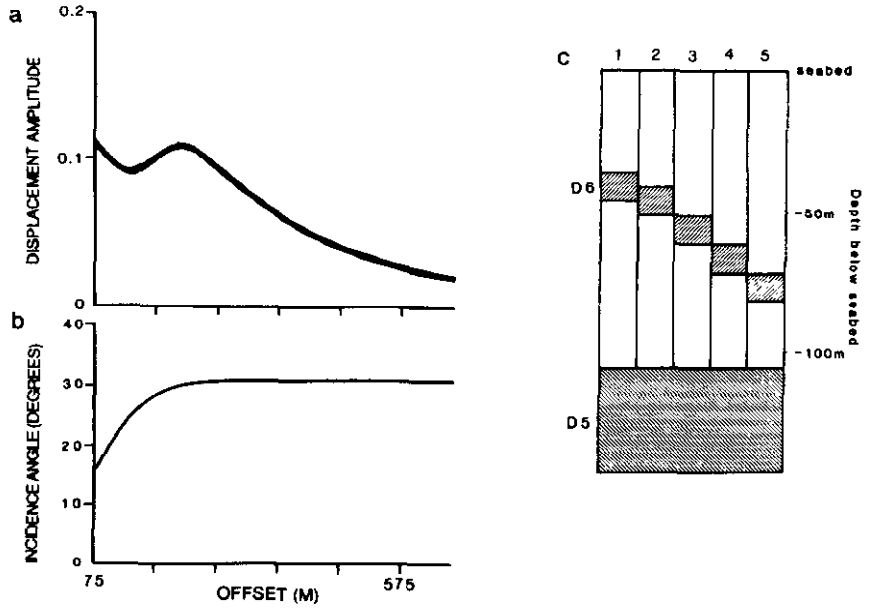

Fig. 7. The effect of variations in the depth of D6 on the amplitude and incidence angle versus source-receiver offset curves for the reflection from the top of D5. All five curves are nearly the same in both **(a)** and **(b)** indicating little to no effect from the depth of D6.

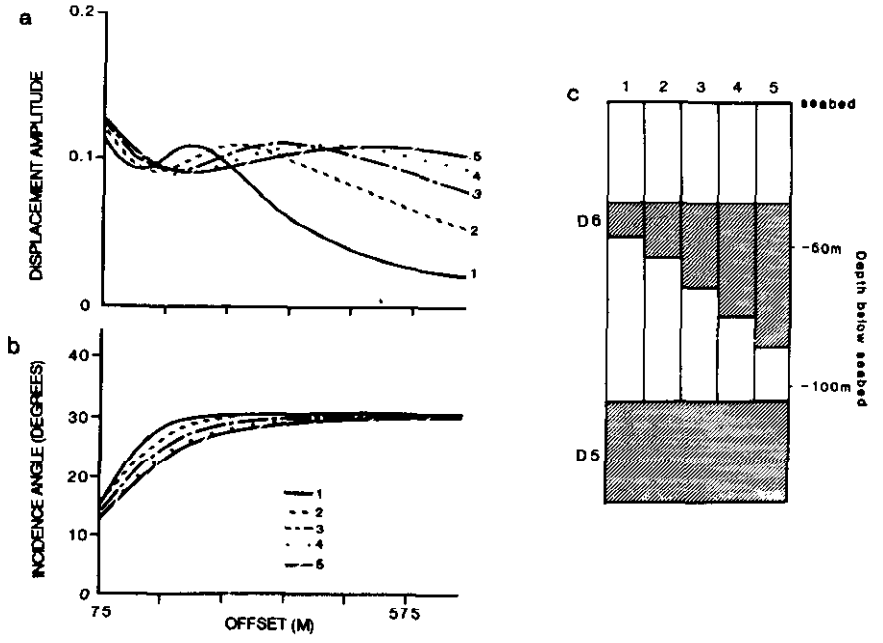

Fig. 8. The effect of variations in the thickness of D6 on the amplitude and incidence angle versus source-receiver offset curves for the reflection for the top of D5.

moveout corrections cannot properly handle events that cross in time-offset space. It is therefore not surprising that the shallow IBPF layer is seldom visible on processed multichannel high-resolution data.

Figure 9b reveals quite a different geometrical relationship for the reflections from the top and bottom of D5 than the case when D6 is present (Figure 5a). The top and bottom reflections converge at the farther offset traces but do not cross for this recording geometry. On the full synthetic seismogram (Figure 5b), reflections from the bases of D5 and D6 as well as the reflection from the top of D5 have traveltimes less than the direct arrival for most traces of the record. A low fold would be obtained for these events when these data are stacked. The basal reflections have the appearance of head waves as their moveout is approximately linear. The arrival time of the head wave from the top of D6 is superimposed on Figure 9a. It is almost coincident with the basal reflection. The basal reflection has significant amplitude due to large incidence angles and could be misinterpreted as a refraction event. It may however be distinguishable due to its negative polarity.

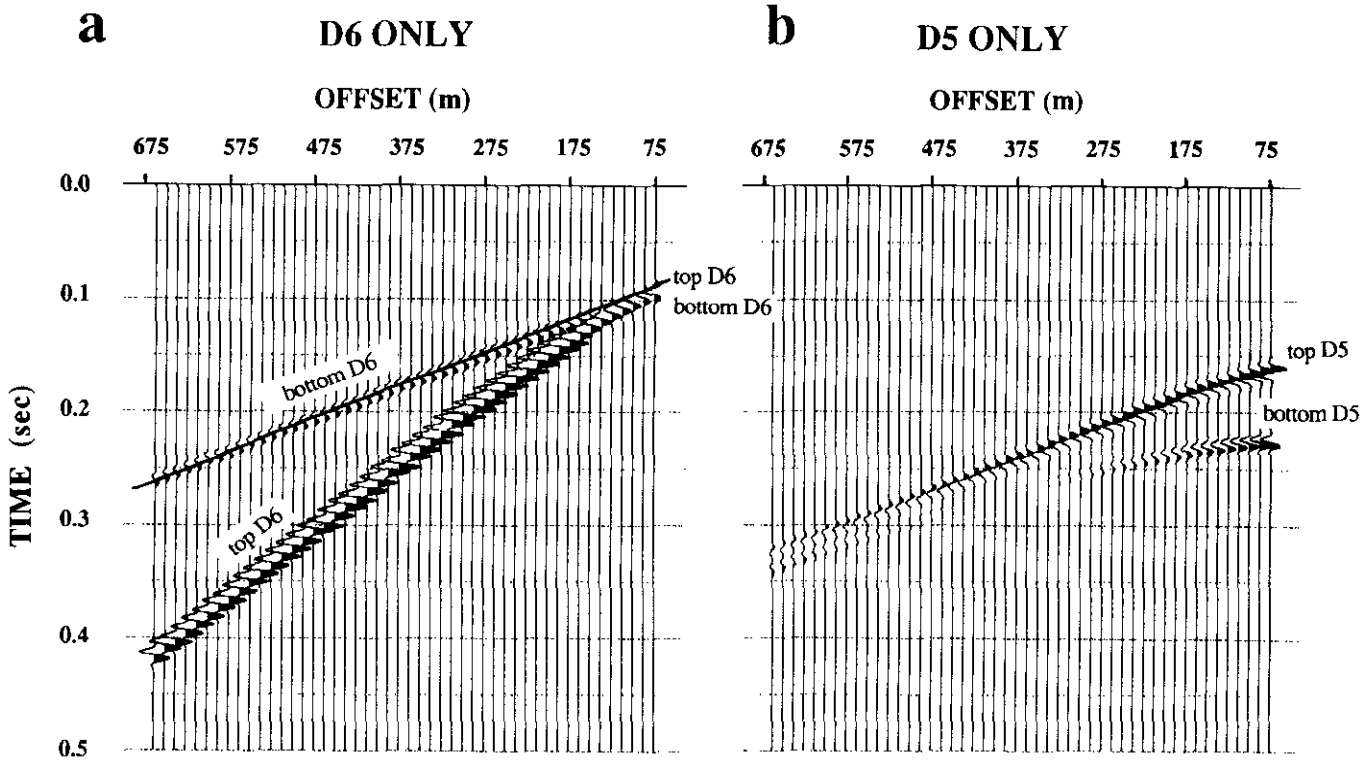

Fig. 9. Synthetic seismograms for the reflections from the top and bottom of D6 **(a)** and D5 **(b)**; the line **(a)** indicates the arrival time of the refraction from the top of D6.

The effect of the shallowest high-velocity layer on the NMO of later reflections is significant. Figure 10a to d is a series of spikegrams for interfaces 2 to 5 of model 2, showing the true arrival times (calculated from ray tracing) as well as those arrival times calculated using the standard NMO equation. Large differences occur between the true and calculated arrival times at the far-offset traces for all interfaces below the top of D6. Although the presence of the shallow high-velocity layer reduces the variations in amplitude with offset of the reflection from the top of the deeper layer, it has a detrimental effect on the moveout curves. Velocity analysis programs based on hyperbolic approximations would pick incorrect velocities for later reflections and the resulting moveout corrections would not flatten these events for stacking.

Significant improvement in the data quality can only be achieved through optimization of recording geometry. A recording geometry which provides high fold at near offsets (i.e., small group interval and/or small shot interval) should be used in areas affected by IBPF. Where this geometry is used, but receivers are long, severe mutes of far-offset energy should be used before stacking the data for imaging of the shallow part of the section.

Conclusions

This paper compares synthetic seismograms from two simplified models representing common juxtaposed distributions of IBPF found in most of the shallow eastern Beaufort Sea continental shelf. Plane-wave modelling, which includes only transmission losses, has been effective in demonstrating many of the inherent problems with data recorded in areas where large velocity contrasts occur in the near surface.

The shallowest layer of IBPF (D6) has a more severe impact on multichannel seismic data than deeper IBPF layers due to the shallow and laterally discontinuous nature of its distribution. In particular:

1. The presence of D6 has the effect of reducing the amplitude and phase variations on the reflection from the top of the D5 IBPF layer. This effect is insensitive to the relative depth of the D6 layer and only slightly sensitive to its thickness.
2. Normal moveout of reflections from interfaces below the top of the shallowest IBPF layer will be nonhyperbolic. Consequently, standard velocity analysis and NMO corrections which assumes hyperbolic moveout will be incorrect.
3. The basal reflection from D6 is almost coincident with the head wave arrival from the top of the layer. It can be distinguished from the refraction by its opposite polarity.
4. The top and bottom reflections from D6 may appear as a single event at near offsets in a shot or CDP gather as well as on stacked sections.
5. In areas of severe velocity contrasts, little improvement can be achieved by reprocessing of existing data that had been recorded with greater than 12.5 m group intervals. A recording geometry which provides high fold at near offsets should be used in areas affected by IBPF.

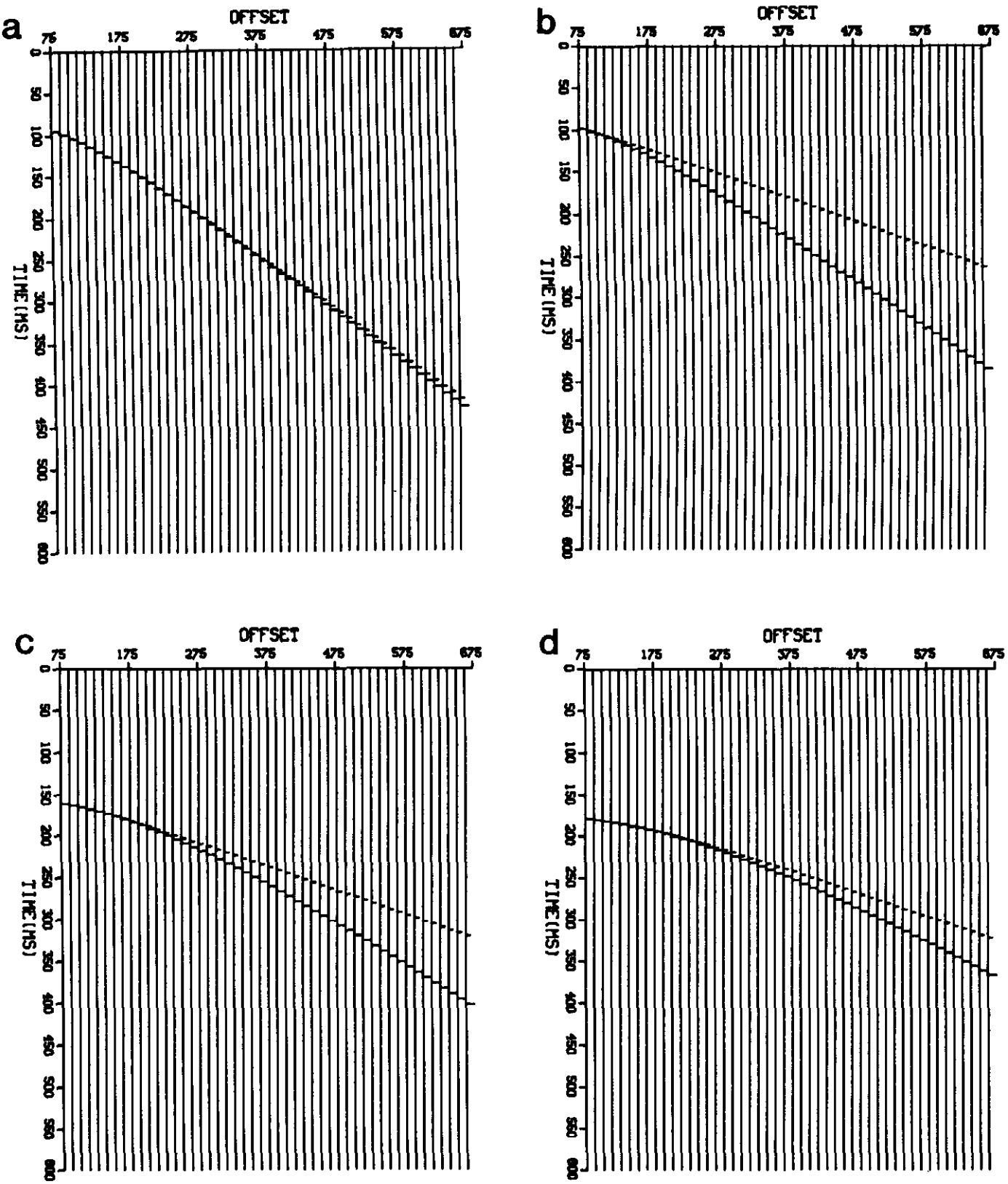

Fig. 10. Spikegrams illustrating the difference between the actual reflection arrival times calculated from ray tracing (small spikes) and those calculated from the RMS velocity, for the reflections from the top and bottom of D6, **(a)** and **(b)** respectively, and the top and bottom of D5, **(c)** and **(d)** respectively.

REFERENCES

Aki, K. and Richards, P.G., 1980, Quantitative seismology, theory and methods: W.H. Freeman & Co.

Blasco, S.M. and O'Connor, M.J., 1981, Acoustic characteristics of subsea permafrost in the southern Beaufort Sea, *in* Proc. 4th Can. Permafrost Conf., Nat. Res. Counc. Can., Calgary.

Earth Physics Branch, 1983, Study of well logs in the Mackenzie Delta - Beaufort Sea to outline permafrost thickness and/or gas hydrate occurrences: Dept. Energy Mines and Resources, Open File 83-10, 1-30.

Fortin, G., 1991, Regional geological framework for the late Neogene/Quaternary strata beneath the Canadian Beaufort continental shelf: Geol. Surv. Can., Open-File Rep., in press.

Gassaway, G.S., 1984, Effects of shallow reflectors on amplitude versus offset (seismic lithology) analysis: 54th Ann. Mtg. and Exposition, Soc. Expl. Geophys., Technical abstracts and biographies, 665-669.

Hamilton, E.L., 1976, Shear-wave velocity versus depth in marine sediments: a review: Geophysics **41**, 895-921.

Hatlelid, W.G. and MacDonald, J.R., 1982, Permafrost determination by seismic velocity analyses: J. Can. Soc. Expl. Geophys. **18**, 14-22.

Hnatnik, J. and Randall, A.G., 1977, Determination of permafrost thickness in wells in northern Canada: Can. J. Earth Sci. **14**, 375-383.

Hunter, J.A., Good, R.L. and Hobson, G.D., 1974, Mapping the occurrence of sub-seabottom permafrost in the Beaufort Sea by shallow refraction techniques: Geol. Surv. Can., Report of Activities Paper 74-1B, 91-94.

King, M.S., Pandit, B.I., Hunter, J.A. and Gajtani, M., 1982, Some seismic, electrical and thermal properties of sub-seabottom permafrost from the Beaufort Sea: Proc. 4th Can. Conf. on Permafrost, Nat. Res. Counc. Can., 268-273.

MacKay, J.R., 1972, Offshore permafrost and ground ice, Southern Beaufort Sea, Canada: Can. J. Earth Sci. **9**, 1550-1561.

Morak, J.L., MacAulay, H.A. and Hunter J.A., 1983, Geophysical measurements of subbottom permafrost in the Canadian Beaufort Sea, *in* Permafrost: 4th international conference, final proceedings: National Academy Press, 866-871.

Neave, K.G., Judge, A.S., Hunter, J.A. and MacAulay, H.A., 1978, Offshore permafrost distribution in the Beaufort Sea as determined from temperature and seismic observations, *in* Current Research, Part C, Geol. Surv. Can., Paper 78-1C.

O'Connor, M.J. and Associates, 1984, Distribution and occurrence of frozen subseabottom sediments — a comparison of geotechnical and shallow seismic evidence from the Canadian Beaufort Sea: Geol. Surv. Can., Internal Report, 1-106.

Osterkamp, T.E. and Payne, M.W., 1981, Estimates of permafrost thickness from well logs in northern Alaska: Cold Regions Science and Technology **5**, 13-27.

Poley, D.F., 1987, Acquisition and processing of high-resolution reflection seismic data from permafrost affected areas of the Beaufort Sea continental shelf: Ph.D. thesis, Univ. of Calgary.

_____, Lawton, D.C. and Blasco, S.M., 1989, Amplitude-offset relationships over shallow velocity inversions: Geophysics **54**, 1114-1122.

Smith, M.W., 1976, Permafrost in the Mackenzie Delta, Northwest Territories: Geol. Surv. Can., Paper 75-28, 1-34.

Timur, A., 1968, Velocity of compressional waves in porous media at permafrost temperatures: Geophysics **33**, 584-595.

Walker, J.H.D. and Stuart, A.J., 1976, Permafrost investigations by crystal cable surveys, Mackenzie Delta, N.W.T.: J. Can. Soc. Expl. Geophys. **12**, 38-55.